FULL PAPER

Magnetic Resonance in Medicine 00:00–00 (2017)

Registration Strategies for Multi-Modal Whole-Body MRI Mosaicing

Jakub Ceranka,[1,2]* Mathias Polfliet,[1,2,3] Frédéric Lecouvet,[4] Nicolas Michoux,[4] Johan de Mey,[5] and Jef Vandemeulebroucke[1,2]

Purpose: To test and compare different registration approaches for performing whole-body diffusion-weighted (wbDWI) image station mosaicing, and its alignment to corresponding anatomical T_1 whole-body image.

Methods: Four different registration strategies aiming at mosaicing of diffusion-weighted image stations, and their alignment to the corresponding whole-body anatomical image, were proposed and evaluated. These included two-step approaches, where diffusion-weighted stations are first combined in a pairwise (Strategy 1) or groupwise (Strategy 2) manner and later non-rigidly aligned to the anatomical image; a direct pairwise mapping of DWI stations onto the anatomical image (Strategy 3); and simultaneous mosaicing of DWI and alignment to the anatomical image (Strategy 4). Additionally, different images driving the registration were investigated. Experiments were performed for 20 whole-body images of patients with bone metastases.

Results: Strategies 1 and 2 showed significant improvement in mosaicing accuracy with respect to the non-registered images ($P < 0.006$). Strategy 2 based on ADC images increased the alignment accuracy between DWI stations and the T_1 whole-body image ($P = 0.0009$).

Conclusions: A two-step registration strategy, relying on groupwise mosaicing of the ADC stations and subsequent registration to T_1, provided the best compromise between whole-body DWI image quality and multi-modal alignment. **Magn Reson Med 000:000–000, 2017. © 2017 International Society for Magnetic Resonance in Medicine.**

Key words: whole-body MRI; MR station mosaicing; image registration; diffusion-weighted MRI; multi-station acquisition

INTRODUCTION

The value of anatomical whole-body MRI is currently investigated in several pathologies, including soft tissue tumour detection (1), diagnosis, and prognosis of multiple mylenoma (2,3), evaluation of the lymph nodes (4) and bone marrow in pediatric age (5). In combination with functional whole-body MR imaging, such as diffusion-weighted MRI (DW-MRI), it allows for lesion characterisation (6), diagnosis of bone involvement by metastases (7,8), and treatment response assessment (9,10).

Because of the MR coil size limitations, whole-body anatomical MRI and whole-body DWI are acquired in separate image segments. Depending on the acquisition, these consist of slabs of two-dimensional (2D) axial slices or three-dimensional (3D) volumes (anatomical sequences) called image stations, which are later combined into a whole-body image. Image stations suffer from inter-station intensity variations (11,12), which have to be corrected in order to obtain a homogeneous whole-body image.

Such intensity standardization between stations has been described previously and will not be considered in this work (13). However, the whole-body MR images often bear additional artifacts at the transition between adjacent stations, caused by patient motion between the acquisition of subsequent stations, and leading to inconsistent anatomical views between stations. Other sources of artifacts include geometric distortions and image shearing caused by eddy currents, induced by rapid switching of gradient coils in echo-planar MR imaging (EPI) sequence; and voxel shifts in the phase-encoding direction in DW images, caused by differences in applied frequency offsets (14). Compensation of such artifacts is the subject of this study.

Geometric artifacts may result in inaccurate representations of the anatomy and yield unreliable morphological measurements, including the size and volume of organs or tumours, or affect the assessment of functional quantities, such as the global apparent diffusion coefficient (ADC) (9). Moreover, the lack of registration between anatomical and functional images may limit or lead to false results in DWI parameters measurements performed on the basis of region of interest defined on anatomical images. It may also compromise the quality of inter-station intensity standardization (ISIS) algorithms—usually driven by the registration of intensity histograms acquired from the image stations or the overlap between the neighbouring image stations (13). In addition, misalignment between multi-modal whole-body MR data hinders visual fusion of the image modalities, thereby limiting the benefits of the combined inspection of function and anatomy.

To compensate for the aforementioned inconsistencies, image stations can be acquired including an overlap of a

[1]Vrije Universiteit Brussel (VUB), Department of Electronics and Informatics (ETRO), Brussels, Belgium.

[2]imec, Leuven, Belgium.

[3]Biomedical Imaging Group, Department of Radiology and Medical Informatics, Erasmus MC, Rotterdam, The Netherlands.

[4]Department of Radiology, Centre du Cancer and Institut de Recherche Expérimentale et Clinique (IREC-IMAG), Cliniques Universitaires Saint-Luc, Université Catholique de Louvain, Brussels, Belgium.

[5]Vrije Universiteit Brussel (VUB), Universitair Ziekenhuis Brussel (UZ Brussel), Department of Radiology, Brussels, Belgium.

*Correspondence to: Jakub Ceranka, Vrije Universiteit Brussel (VUB), Department of Electronics and Informatics (ETRO), Pleinlaan 2, 1050 Brussels, Belgium. E-mail: jceranka@etrovub.be.

Received 8 December 2016; revised 26 April 2017; accepted 23 May 2017

DOI 10.1002/mrm.26787

Published online 00 Month 2017 in Wiley Online Library (wileyonlinelibrary.com).

predefined length between neighbouring segments. Mosaicing of the whole-body image stations and aligning them to their multi-modal corresponding image using image registration remains a challenging task, in particular for DW-MRI. These functional images have relatively low spatial resolution (slice thicknesses above 5 mm are common), poor signal-to-noise ratio (SNR) and the overlapping regions are often limited to a few slices (15). In addition, prior to ISIS, voxel intensities cannot be compared directly for whole-body mosaicing or alignment with other MR modalities. In many cases, whole-body anatomical (e.g., T_1 or T_2-weighted) MRI is acquired during the same session. Such anatomical MR images have comparatively high spatial resolution and are not affected by DWI related image distortions, which make them reliable anatomical reference images.

To date, three approaches have been proposed aimed at solving related registration problems to the one described above. Blackledge et al. (9) proposed a sequential station-to-station registration algorithm for diffusion-weighted MR, compensating for uni-dimensional translations along phase-encoding direction. The registration was applied to DW b1000 image stations, and driven by a mean squared differences (MSD) metric after applying ISIS. Alignment with the anatomical MRI was not addressed. Others have described registering pre and post treatment DWI scans of different *b*-values, using a non-rigid registration (8,10), but the method was not presented in detail. Dzyubachyk et al. proposed a gradient-based registration approach for the reconstruction of the complete spine from high-quality, anatomical multi-station 7T MR images, but the approach is unsuited for the current problem, where gradient image information does not correspond between DWI and anatomical MR stations, and stations consist of low-resolution, noisy DW images (16).

In this study, we compare four registration strategies for whole-body MR image mosaicing and functional to anatomical whole-body image alignment. To the best of our knowledge, the aforementioned problem has not yet been addressed in the literature. In addition to the evaluation of different registration strategies, the influence of the choice of image channel (high *b*-value, low *b*-value or ADC image) and similarity measures are evaluated. Experiments are performed on whole-body, multi-modal MR acquisitions of patients with bone metastases.

THEORY

Image Registration

Image registration is commonly performed in a pairwise manner, where the aim is to find the transform $\mathcal{T}_{\boldsymbol{\mu}}$, that aligns the moving image g to the fixed or reference image f. As such, it can be described by the following optimization problem over the parameters $\boldsymbol{\mu}$ of the spatial transformation $\mathcal{T}$

$$\hat{\boldsymbol{\mu}} = \arg \min_{\boldsymbol{\mu}} \mathcal{C}_{\boldsymbol{x}\in\Omega}(f(\boldsymbol{x}), g(\mathcal{T}_{\boldsymbol{\mu}}(\boldsymbol{x}))) . \quad [1]$$

In (1), the spatial coordinate $\boldsymbol{x}$ is taken from the overlapping region Ω, in which we assumed an intensity interpolation scheme for the discrete images f and g. The registration is guided by the minimization of the chosen cost function $\mathcal{C}$, typically defined as a weighted sum of a (dis)similarity metric, $\mathcal{D}$, and a regularizer, $\mathcal{R}$ with associated weight α

$$\mathcal{C} = \mathcal{D} + \alpha\mathcal{R} . \quad [2]$$

Aligning multiple images can be achieved by sequentially applying pairwise registration to a chosen reference image. An alternative is the so-called groupwise approach, in which a set of n images, f_i, are simultaneously aligned, by jointly optimizing n spatial transformations $\mathcal{T}_{\mu^i}$,

$$\theta = \arg \min_{\boldsymbol{\mu}} \mathcal{C}_{\boldsymbol{x}}(f_1(\mathcal{T}_{\boldsymbol{\mu}_1}(\boldsymbol{x})), \ldots, f_n(\mathcal{T}_{\boldsymbol{\mu}_n}(\boldsymbol{x}))) . \quad [3]$$

Here, θ is now a concatenated vector of $\boldsymbol{\mu}_i$. Registration using (3) considers all image information simultaneously, and does not require choosing a reference image, thereby avoiding bias. Since an infinite amount of equivalent solutions to (3) exist, an extra constraint can be introduced, commonly set to

$$\frac{1}{n}\sum_{i=1}^{n} \mathcal{T}_{\boldsymbol{\mu}_i}(\boldsymbol{x}) = \boldsymbol{x}, \;\; \boldsymbol{x} \in \Omega . \quad [4]$$

Latter constraint minimizes the total image deformation of the set of images, which effectively maps them to a mean reference space (17).

The registration strategies are based on rigid and a B-spline deformation model. The rigid image transformation model $\mathcal{T}_{\boldsymbol{\mu}}$ is defined as a transformation of image coordinates from the fixed image domain f to a moving image g considering six degrees-of-freedom, consisting of three translation parameters and thee rotation angles. The B-spline deformable transformation (18) can be defined as

$$\mathcal{T}_{\boldsymbol{\mu}}(\boldsymbol{x}) = \boldsymbol{x} + \sum_{\boldsymbol{x}_k \in N_{\boldsymbol{x}}} \boldsymbol{p}_k \beta^n(\boldsymbol{x} - \boldsymbol{x}_k), \quad [5]$$

where $\boldsymbol{x}$ is a spatial coordinate of the 3-dimensional image, $\boldsymbol{x}_k$ is the set of control points defined on a 3D regular grid spanning the image, $\boldsymbol{p}_k$ are the B-spline coefficient vectors, $\beta^n(x)$ are the nth order multidimensional B-spline polynomial. $N_{\boldsymbol{x}}$ is the set of all control points with non-zero B-splines at the voxel position $\boldsymbol{x}$.

Dissimilarity Metrics

Due to different MR image modalities used (i.e., DWI and T_1) and intensity scale differences within the same modality (between DWI image stations), each registration approach has to be tailored with a suitable metric.

The most straightforward metric involves the computation of mean squared differences ($\mathcal{D}_{\mathrm{MSD}}$) of the overlapping image intensities

$$\mathcal{D}_{\mathrm{MSD}}(f, g(\mathcal{T}_{\boldsymbol{\mu}}) = \sum_{\boldsymbol{x}\in\Omega} \frac{\left(f(\boldsymbol{x}) - g\left(\mathcal{T}_{\boldsymbol{\mu}}(\boldsymbol{x})\right)\right)^2}{N_\Omega} . \quad [6]$$

Here, N_Ω is a number of voxels in the image overlay. $\mathcal{D}_{\mathrm{MSD}}$ assumes a one-to-one intensity correspondence,

and therefore cannot be directly applied to the multi-modal data or data suffering from intensity scale differences.

The groupwise extension of the $\mathcal{D}_{\mathrm{MSD}}$, which we will refer to as averaged mean squared differences $\mathcal{D}_{\mathrm{AMSD}}$ (19), is defined as

$$\mathcal{D}_{\mathrm{AMSD}}(f_1(\mathcal{T}_{\boldsymbol{\mu}_1}),\ldots,f_n(\mathcal{T}_{\boldsymbol{\mu}_n})) = \sum_{i=1}^{n} \mathcal{D}_{MSD}(f_i(\mathcal{T}_{\boldsymbol{\mu}_i}(\boldsymbol{x})),\bar{f}_{\boldsymbol{\theta}}(\boldsymbol{x}))\,, \quad [7]$$

where, $\bar{f}_{\boldsymbol{\theta}}$ is an arithmetic mean intensity image defined as

$$\bar{f}_{\boldsymbol{\theta}}(\boldsymbol{x}) = \frac{1}{n}\sum_{i=1}^{n} f_i(\mathcal{T}_{\boldsymbol{\mu}_i}(\boldsymbol{x}))\,. \quad [8]$$

In case of data with linear intensity scale differences or intensity off-set, a solution would be to standardize the inter-station intensities prior to the registration and use $\mathcal{D}_{\mathrm{MSD}}$ (or $\mathcal{D}_{\mathrm{AMSD}}$); or employ a metric assuming a linear correspondence between voxel intensities, such as normalized cross correlation ($\mathcal{D}_{\mathrm{NCC}}$),

$$\mathcal{D}_{\mathrm{NCC}}(f, g(\mathcal{T}_{\boldsymbol{\mu}}) = \sum_{\boldsymbol{x}\in\Omega} \frac{\big(f(\boldsymbol{x}) - m_f\big)\big(g(\mathcal{T}_{\boldsymbol{\mu}}(\boldsymbol{x})) - m_g\big)}{\sigma_f \sigma_g}. \quad [9]$$

In (9), m_f and m_g respectively are the mean intensities of the reference and the target image, and σ_f and σ_g are their variances.

For alignment of multi-modal data, mutual information is commonly used ($\mathcal{D}_{\mathrm{MI}}$) (20), which is defined as follows:

$$\mathcal{D}_{\mathrm{MI}}(f, g(\mathcal{T}_{\boldsymbol{\mu}}) = -\sum_{a,b} p_{fg}(a,b)\log\ \frac{p_{fg}(a,b)}{p_f(a)p_g(b)}\,, \quad [10]$$

where p_{fg} is the joint probability density function (PDF) of the intensity functions f and g, and p_f and p_g are the marginalised PDFs for the respective images. a and b are the discretized image intensity values.

In order to handle multi-modal data in a groupwise approach, pairwise $\mathcal{D}_{\mathrm{MI}}$ metric can be extended to the average mutual information metric ($\mathcal{D}_{\mathrm{AMI}}$) (17,21)

$$\mathcal{D}_{\mathrm{AMI}}(f_1(\mathcal{T}_{\boldsymbol{\mu}_1}),\ldots,f_n(\mathcal{T}_{\boldsymbol{\mu}_n})) = \sum_{i=1}^{n} \mathcal{D}_{MI}(f_i(\mathcal{T}_{\boldsymbol{\mu}_i}(\boldsymbol{x})),\bar{f}_{\boldsymbol{\theta}}(\boldsymbol{x}))\,. \quad [11]$$

Alternatively, if two or more DWI b-values are available, one can compute the apparent diffusion coefficient images (ADC), according to

$$\mathrm{ADC}(\boldsymbol{x}) = \frac{1}{(b_1 - b_0)}\ln\frac{f_0(\boldsymbol{x})}{f_1(\boldsymbol{x})}\,, \quad [12]$$

where, $f_0(\boldsymbol{x})$ and $f_1(\boldsymbol{x})$ are the image intensities in the given voxel position $\boldsymbol{x}$ and b_0, b_1 are b-values of chosen images. In theory, ADC images are less susceptible to shine-through artifacts and inter-station intensity scale differences. As such, they represent quantitative voxel intensity values, which can be directly compared across stations. The use of ADC images may improve registration results as they allow for the use of simpler, one-to-one comparison of image intensities by the means of $\mathcal{D}_{\mathrm{MSD}}$ registration metric. Preliminary results obtained in previous work confirm latter hypothesis (22). We found that mosaicing using rigid registration, driven by $\mathcal{D}_{\mathrm{MSD}}$ between the ADC maps obtained from DWI stations, outperformed registration using $\mathcal{D}_{\mathrm{MI}}$ and $\mathcal{D}_{\mathrm{NCC}}$, and approaches described in literature (9).

METHODS

Population

Experiments were performed on retrospective patient data, consisting of whole-body 3D T_1 *anatomy* images and *functional* whole-body diffusion-weighted images (wbDWI). Twenty whole-body, multi-modal image pairs of 11 prostate cancer patients with bone metastases were used, each patient having from 1 to 4 follow-up examinations, with 3–9 months between consecutive scans. Images were acquired using Philips Ingenia Medical Systems 3T MR imaging system at the Cliniques Universitaires Saint-Luc (Brussels, Belgium), as routine examination performed in patients with different stages of metastatic bone disease. The retrospective study was approved by the Institutional Ethics Board of the Cliniques Universitaires Saint-Luc. All images were anonymised before archiving and post-processing. Whole-body anatomical and DW images were obtained by sequential acquisition of four image stations, roughly covering legs, pelvis, torso and head. Both modalities were obtained during the same scanning session, first anatomy, followed by diffusion-weighted images.

MRI

3D T_1-weighted spin-echo sequence (23) with the following sequence parameters was used: repetition time (TR) = 382–546 ms, echo time (TE) = 8–20 ms, slice thickness 1.19–4.40 mm, matrix size of 480 × 480–500 × 500, pixel spacing 0.65–0.93 mm, field of view (FOV) = 480 × 480–768 × 768 mm^2.

Diffusion weighted-images (i.e., trace or isotropic diffusion image) were acquired with axial free breathing echo-planar diffusion-weighted sequence [DWIBS (15)] with 1 average across 3 directions (x, y, z). Eight scans with two ($b = 0$, 1000 s/mm^2), four scans with three ($b = 0$, 150, 1000 s/mm^2) and eights scans with four ($b = 0$, 50, 150, 1000 s/mm^2) b-values were obtained. ADC maps were calculated using a mono-exponential fit across all available b-values for a given DWI scan. Following sequence parameters were used: TR = 8421 ms, TE = 66 ms, slice thickness 6.1 mm, matrix size of 192 × 192, pixel spacing 2.3 mm, FOV = 440 × 440 mm^2. The modality has 5 slices of the overlap region between two neighbouring stations. The total acquisition time for anatomical and functional whole-body images was around 50 min.

Inter-Station Intensity Standardization

Prior to the registration based on the MSD metric, the intensity of the DWI b0 stations was standardized. The

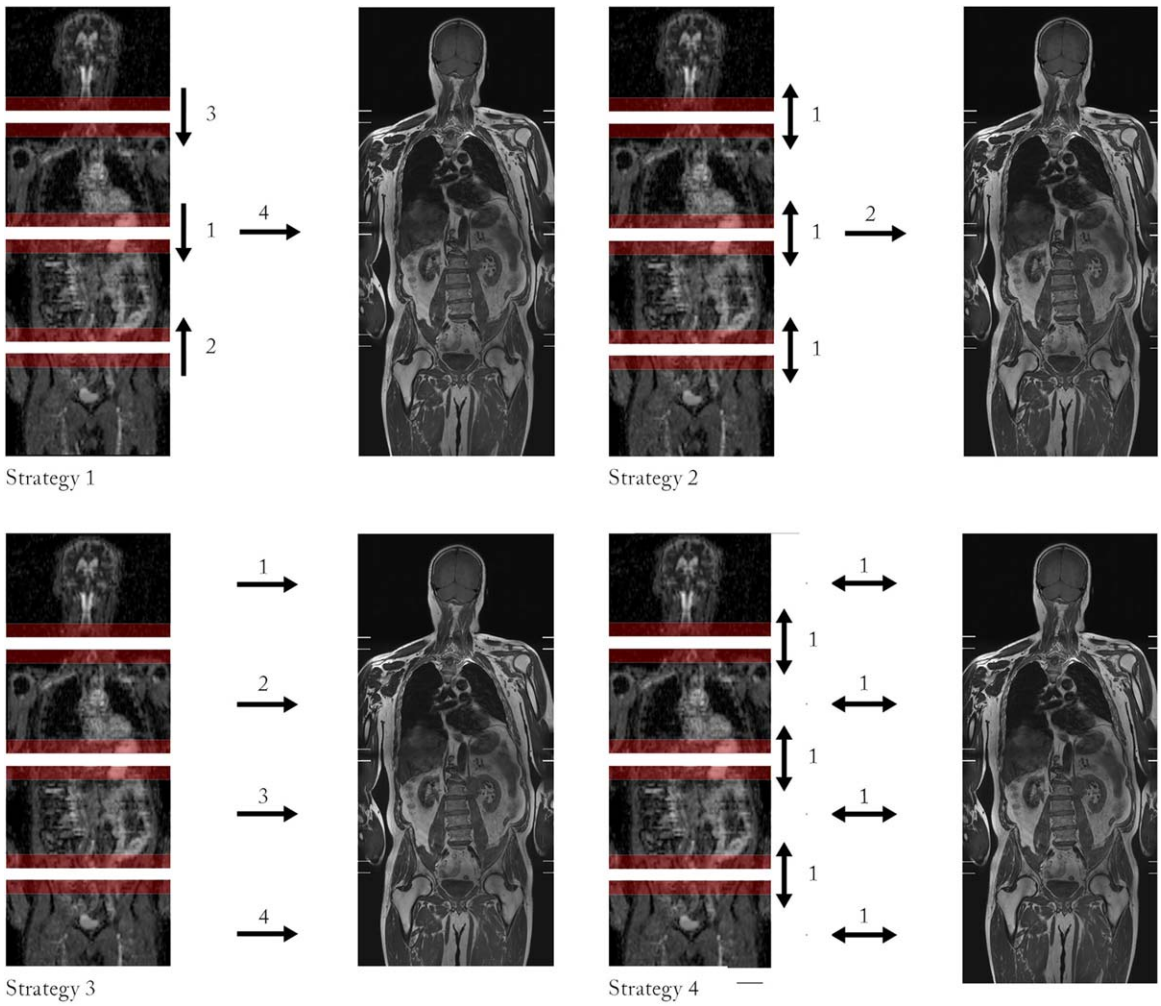

FIG. 1. Schematic illustration of the different registration strategies proposed for whole-body DW image mosaicing and alignment to 3D-T_1 whole-body reference image. Numbers next to arrows indicate the order of applied steps. Strategy 1: First, diffusion-weighted stations are sequentially aligned to a reference station (pelvis) forming a whole-body image (pairwise approach). Secondly obtained wbDWI image is deformably aligned using mutual information to the corresponding T_1-weighted anatomical reference. Strategy 2: Simultaneous optimization of all DW image stations position (groupwise approach), followed by deformable registration to anatomical reference. Strategy 3: DW image stations are directly, deformably registered to a T_1 whole-body anatomical image. Strategy 4 and 4′: Mosaicing of DWI whole-body image with simultaneous, deformable alignment to T_1 whole-body anatomical image.

inter-station intensity standardization algorithm was adapted from Nyul et al. (12), and based on histogram matching of the reference and target image overlap regions. The Insight Segmentation and Registration Toolkit (ITK) (24) implementation of the method was used and modified to compute histograms only from the image station overlay region. Histograms were matched according to 13 automatically selected points of the histogram, corresponding to the quartile and deciles values. The target image histogram landmarks were then adjusted to match the histogram landmarks of the reference image and the target image intensities were standardized according to obtained piecewise linear transform functions. The algorithm optimizes the intensity scaling factor by minimizing the mean squared error between the histogram nodes. Station intensities were corrected in a pairwise and sequential manner, taking the centrally located pelvis station as the first reference image to minimize the cumulative error.

Registration Strategies

Whole-body MR images are automatically constructed by Ingenia Philips Scanner software, with manual station-intensity correction done by an MR technician. Due to the high resolution and SNR of the image stations, the T_1 whole-body images provided by the scanner vendor were of excellent quality. Therefore, mosaicing of T_1-weighted image stations was not further investigated. Only mosaicing of DWI stations and alignment to T_1 was considered.

Four registration strategies were compared (see Fig. 1) in this study. Except for strategy *S*4′, all strategies were initialized starting from the raw, non-registered image positions.

- **Strategy 1 (*S*1)**: In a first step, wbDWI mosaicing is performed by sequential, pairwise registration of neighbouring stations, taking the centrally located pelvis station as a reference image in order to

minimize the cumulative registration error. Registration was performed rigidly, on the overlapping boundary of each image station. In a second step rigid and then deformable mapping of wbDWI image to T_1-weighted whole-body is performed.

- **Strategy 2 (*S2*)**: In this case, a groupwise simultaneous mosaicing approach for DWI stations is employed instead of the sequential pairwise approach used above. Next, the obtained whole-body DW image is rigidly and deformably aligned to T_1 whole-body anatomical reference.
- **Strategy 3 (*S3*)**: Direct deformable registration of DWI image stations onto T_1 whole-body anatomical reference is performed using a sequential pairwise approach between DWI segment and T_1. The alignment of neighbouring DWI segments is not explicitly considered in the registration metric. Instead it is assumed that registration of DWI stations onto the whole-body anatomical reference will lead to wbDWI with high image continuity.
- **Strategy 4 (*S4*)**: Here, simultaneous deformable registration of all DWI segments to the T_1 whole-body anatomical reference is attempted using a groupwise approach, and based on a metric which considers both DWI station mosaicing and alignment with T_1.
- **Strategy 4′ (*S4′*)**: Joint cost function optimization strategies are usually more sensitive to initialization. Therefore, a modification of the Strategy *S*4 was additionally implemented. Here, the same joint optimization scheme as in Strategy *S*4 was used, but the Strategy *S*4′ was initialized with the result of the best performing method assessed by the rank in overall registration accuracy.

For two-step approaches, *S*1 and *S*2, the whole-body DWI mosaicing and the alignment to the anatomical reference is performed separately. As such, stations are constrained to a certain relative position or pose, and only afterwards (non-rigidly) mapped to the whole-body reference, which may reduce the attainable accuracy with respect to direct approaches *S*3 and *S*4. The potential advantage may come from the fact that individual registration steps become less complex, considering less degrees of freedom, and offering the possibility to use a metric (in particular in the first step) which assumes a more direct relationship between the intensity distributions, such as $\mathcal{D}_{\mathrm{MSD}}$.

Groupwise approaches, as in *S*2 and *S*4, consider all image information and degrees of freedom simultaneously, resulting in increased complexity with respect to (sequential) pairwise approaches, as in *S*1 and *S*3. On the other hand, such approaches avoid cumulative registration errors, and allow minimizing the overall transformation using Equation [4], effectively reducing whole-body image tilt.

Each of the registration approaches was applied on ADC and b0 diffusion-weighted image stations, with different metrics depending of the used technique. A DWI b0 image delivers a T_2-weighted EPI diffusion-weighted image for anatomical reference which does not increase the contrast in pathogenic regions (as in DWI b-1000) and additionally shows higher resemblance to anatomical sequences. Previous experiments (22) performed on high *b*-value images showed considerably worse results, and will not be described further. For the detailed description of all registration components, see Table 1.

The same method for assembling image stations into a whole-body image was used for each registration strategy. All stations were mapped on a reference 3D frame, and the overlap region was evenly split between the two neighbouring stations. No intensity blending was applied on the station-to-station overlap region, allowing for evaluation of the smoothness of the transition between the stations of the resulting whole-body image.

Registration algorithms were implemented in elastix (25) using the adaptive stochastic gradient descent optimizer, with 2048 randomly selected samples (8192 in case of the groupwise step of *S*2 and *S*4 strategy) and 2000 iterations for each level of the multiresolution scheme. The implementations included two resolution levels for rigid registrations followed by three resolution levels for B-spline registrations. For deformable registration, regularization using a bending energy penalty was used (18). The regularisation weight was chosen empirically through visual comparison of the obtained registration results. Multiple weights were tested in the range of [0–200] for strategies *S*1 and *S*2. A value of 100 was found to give the best compromise (with the weight of the similarity metric set to 1), and this value was selected for all registration strategies and subjects. The detailed implementation of a groupwise $\mathcal{D}_{\mathrm{AMI}}$ metric is described in (21).

Evaluation Criteria

Mosaicing accuracy of the whole-body DWI image was assessed in the station overlapping region by three measures and one metric was used to measure the alignment accuracy between DWI and T_1 image (see Fig. 2). For the consistency of evaluation and image visualization, all registered DWI images were mapped to T_1 reference space.

- **Mean Absolute Difference** (*MAD*): Corresponding voxel intensities in the registered image stations overlay regions were compared and summed in absolute value, i.e., for pairwise registration

$$\mathrm{MAD} = \frac{1}{k}\sum_{i=1}^{k}\frac{\sum_{\boldsymbol{x}\in\Omega_i}|f(\boldsymbol{x}) - g(\mathcal{T}_{\boldsymbol{\mu}}(\boldsymbol{x}))|}{N_{\Omega_i}}, \qquad [13]$$

where, $f(\boldsymbol{x})$ and $g(\mathcal{T}_{\boldsymbol{\mu}}(\boldsymbol{x}))$ are image intensities of the reference and transformed, neighbouring ADC image stations at the corresponding voxel location $\boldsymbol{x}$ in the overlapping region Ω_i and N_{Ω_i} is a number of voxels in that station-to-station overlay region. The average of MAD was calculated out of k station overlay regions present in whole-body DWI image ($k = 3$).

- **Intensity edge map along Z-direction (EM_Z)**: The partial derivative along the cranio-caudal direction of the mosaicked ADC whole-body image was calculated using a 3D Sobel kernel, resulting in a cranio-caudal edge map. Average voxel intensity at the

Table 1
Registration Strategies Compared in the Study

		Step 1: Whole-body DWI mosaicing					Step 2: DWI to T_1 alignment			
Registration strategy	Symbol	Type	Image stations	Metric	ISIS	$\mathcal{T}_\mu$[a]	Type	Image	Metric	$\mathcal{T}_\mu$[b]
Strategy 1	$S1^{MSD}_{ADC}$	Pairwise	ADC[c]	$\mathcal{D}_{MSD}$	No	R[h]	Pairwise	wb-ADC[e] and T_1[g]	$\mathcal{D}_{MI}$	R+B[i]
	$S1^{MSD}_{b0}$	Pairwise	b0[d]	$\mathcal{D}_{MSD}$	Yes	R	Pairwise	wb-b0[f] and T_1	$\mathcal{D}_{MI}$	R+B
	$S1^{NCC}_{b0}$	Pairwise	b0	$\mathcal{D}_{NCC}$	No	R	Pairwise	wb-b0 and T_1	$\mathcal{D}_{MI}$	R+B
Strategy 2	$S2^{MSD}_{ADC}$	Groupwise	ADC	$\mathcal{D}_{AMSD}$	No	R	Pairwise	wb-ADC and T_1	$\mathcal{D}_{MI}$	R+B
	$S2^{MSD}_{b0}$	Groupwise	b0	$\mathcal{D}_{AMSD}$	Yes	R	Pairwise	wb-b0 and T_1	$\mathcal{D}_{MI}$	R+B
Strategy 3	$S3^{MI}_{ADC}$						Pairwise	ADC and T_1	$\mathcal{D}_{MI}$	R+B
	$S3^{MI}_{b0}$						Pairwise	b0 and T_1	$\mathcal{D}_{MI}$	R+B
Strategy 4	$S4^{AMI}_{ADC}$	Groupwise R+B using $\mathcal{D}_{AMI}$ on ADC stations and T_1 image								
	$S4^{AMI}_{b0}$	Groupwise R+B using $\mathcal{D}_{AMI}$ on b0 stations and T_1 image								
Strategy 4′	$S4'^{AMI}_{ADC}$	Groupwise R+B using $\mathcal{D}_{AMI}$ on ADC stations and T_1 image, initialized with $S2^{MSD}_{ADC}$								
	$S4'^{AMI}_{b0}$	Groupwise R+B using $\mathcal{D}_{AMI}$ on b0 stations and T_1 image, initialized with $S2^{MSD}_{ADC}$								

[a]Transformation model in Step 1.
[b]Transformation model in Step 2.
[c]Separate ADC image stations.
[d]Separate b0 image stations.
[e]Whole-body ADC image constructed in Step 1.
[f]Whole-body b0 image constructed in Step 1.
[g]Whole-body T_1 anatomy.
[h]Rigid registration transform.
[i]Rigid followed by B-spline deformation registration transform.

station overlay region was calculated, as a measure for the smoothness of the transition between two neighbouring stations (see Fig. 3). The edge intensity is expected to result in higher values for images with inconsistent views at the interface.

- **Dice coefficient of the spinal cord (DC_{SP})**: The spinal cord structure was manually delineated from raw b0 head, torso, and pelvis segments, prior to the registration. The Dice coefficient was used as a measure to evaluate the spatial overlap accuracy of

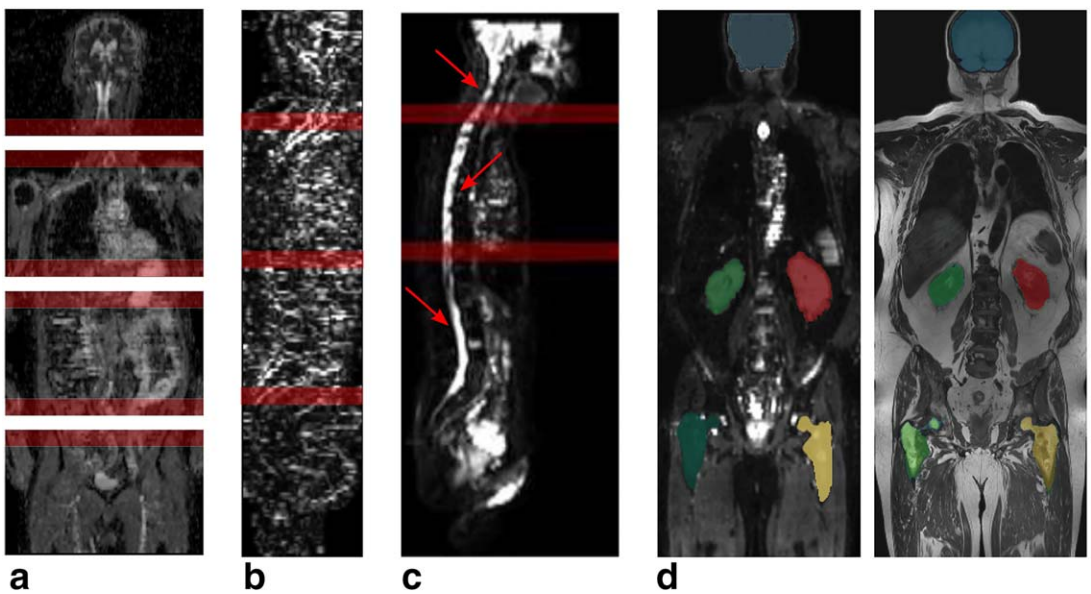

FIG. 2. Visual representation of the used evaluation criteria. **a**: Registered ADC image stations with the overlay region marked in red. Averaged mean absolute differences in the inter-station overlay region was measured. **b**: Edge image calculated along cranio-caudal direction from mosaicked ADC whole-body image. Average edge intensity was measured in the inter-station overlay region (red). **c**: b0 whole-body image. The spinal cord was manually segmented from head, torso, and pelvis b0 image stations prior to the registration (red arrows). Alignment of the segmented structures was evaluated using the Dice coefficient in the station overlay region (red). **d**: Five different organs were manually segmented from the whole-body T_1 (right) and the corresponding DWI image (left) prior to the registration. Inter-modality organ alignment accuracy was measured with the Dice coefficient.

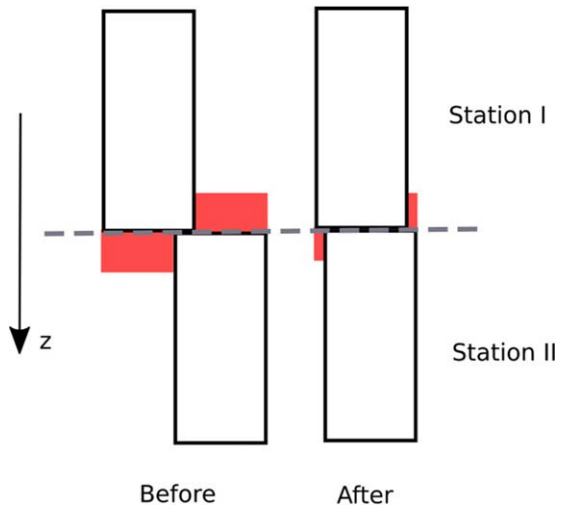

FIG. 3. Example of the behaviour of intensity edge map along Z-direction. A rectangular structure spread across two image stations is shown before and after the registration. Improved alignment of the stations will result in improved inter-station image continuity, generating less axial edges at the interface between stations (red).

delineated spinal cord between transformed neighbouring stations in the overlay region. The Dice coefficient DC is a the similarity measure, which compares two binary objects F, G

$$DC(F,G) = \frac{2|F \cap G|}{|F| + |G|}. \quad [14]$$

The average of DC_{SP} calculated from the overlay regions was obtained.

- **Dice coefficient between corresponding organs (DC_O)**: The alignment accuracy between diffusion-weighted stations and the whole-body anatomical image was measured by multiple organ Dice similarity metric. Five corresponding organs were manually segmented from non-registered DWI b0 stations and the whole-body T_1 image, independently. This included the brain, two kidneys, and two femur bones. After image registration, the delineated ROIs were warped with the obtained transforms and their alignment was evaluated by the Dice coefficient and averaged across organs to evaluate the inter-modality alignment accuracy.

Since not all of the data proved to be normally distributed [$P > 0.05$, Shapiro-Wilk Normality Test (26)], the Wilcoxon two-tailed, signed-rank test was used to investigate statistical significance of differences in validation criteria values between the raw unregistered images and each of the registration strategies separately. Statistical significance with P-value equal to 0.006 (0.05 after Bonferroni correction for the multiple comparisons that are performed) was evaluated to show potential improvement in image alignment. In order to test statistical significance between results of the same registration strategy driven by a different image, P-value equal to 0.05 was used.

In order to summarize the wbDWI image mosaicing quality, the following procedure was applied. First, for each of the evaluation criteria, the ranks of each strategy were computed per patient. Next, the ranks of the three corresponding metrics were averaged for each patient to yield one measure for mosaicing quality per patient, and averaged over all patients. In case of whole-body DWI to T_1 image alignment, since there was only one validation criterion, the ranks were simply averaged over all patients.

RESULTS

All proposed registration strategies were quantitatively validated and compared to a non-registered, raw whole-body image, representing a baseline value. Results were divided into two groups: measures describing accuracy of the whole-body DWI image mosaicing and measures describing multi-modal whole-body alignment of DWI and T_1 whole-body image.

Results of the validation criteria for mosaicing accuracy of whole-body DWI image and alignment accuracy between diffusion-weighted and anatomical whole-body MR images, averaged over all patients, are presented in Table 2. Figure 4 illustrates the distribution of the results of different registration strategies for each of the applied validation criteria.

Figure 5 shows the relation between average rank for whole-body DW image mosaicing quality and the rank of the multi-modal alignment accuracy. The effect of the registration on reconstructed whole-body DW images is presented in Figure 6.

Strategies implemented as a two-step approach (i.e., $S1$ and $S2$), where the wbDWI was first mosaicked and later aligned to its anatomical counterpart, consistently led to improved wbDWI registration quality. Strategies using a direct approach, where DW stations were mapped onto whole-body anatomical image without ($S3$) or by taking into account ($S4$) the DW image station alignment, often gave worse results then the unregistered raw whole-body images. Visually, the wbDWI images showed strong image discontinuities and unrealistic deformations (see Fig. 6). To ascertain that the poor performance of the joint optimization strategy $S4$ was not caused by the imprecise initialization, we verified its performance when initialized with the result of the best performing strategy, i.e., $S2^{\mathrm{MSD}}_{\mathrm{ADC}}$. The results of strategy $S4'$, showed significant improvement compared to strategy $S4$ ($P < 0.021$). However, the results of the two-step strategy $S2$ were still better than $S4'$ ($P < 0.001$).

For the two-step approaches ($S1$ and $S2$), multi-modal image alignment accuracy between whole-body DWI and T_1 images has significantly increased only in case of $S2$, using ADC images ($P = 0.00089$), DC_O criterion. Mosaicing performed using strategy $S1$ resulted in image tilting towards the front, which may have compromised the multi-modal registration accuracy. For direct approaches, the organ similarity metric for DWI to anatomical image alignment showed significant improvement only for strategy $S3^{\mathrm{MI}}_{\mathrm{ADC}}$ ($P < 0.00025$).

The difference between using ADC or b0 images was significant in the case of DWI image mosaicing accuracy for strategy $S1$ ($P < 0.014$). However, the strategies using

Table 2
Evaluation Metrics Averaged Over 20 Whole-Body Images for the Proposed Strategies (± Standard Deviation).

Registration strategy		wbDWI mosaicing						DWI to T_1	
		MAD	$P \times 10^{-3}$	EM_Z	$P \times 10^{-3}$	DC_{SP}	$P \times 10^{-3}$	DC_O	$P \times 10^{-3}$
	Raw	438.2 ± 40.4		1337.7 ± 211.6		0.32 ± 0.10		0.67 ± 0.07	
Strategy 1	$S1^{MSD}_{ADC}$	346.2 ± 33.6	0.089	1278.4 ± 201.1	0.120	0.71 ± 0.11	0.088	0.67 ± 0.06	151.1
	$S1^{MSD}_{b0}$	**340.0 ± 33.9**	0.089	1651.2 ± 243.0	0.089	**0.76 ± 0.07**	0.088	0.58 ± 0.09	0.341
	$S1^{NCC}_{b0}$	342.5 ± 34.8	0.089	1655.7 ± 253.6	0.089	0.74 ± 0.10	0.088	0.58 ± 0.09	0.189
Strategy 2	$S2^{MSD}_{ADC}$	404.7 ± 50.6	0.593	**1214.5 ± 175.6**	0.089	0.69 ± 0.11	0.088	0.77 ± 0.06	0.886
	$S2^{MSD}_{b0}$	413.9 ± 36.5	3.600	1567.2 ± 209.1	0.089	0.70 ± 0.12	0.088	0.69 ± 0.08	218.0
Strategy 3	$S3^{MI}_{ADC}$	481.4 ± 36.5	0.219	1599.0 ± 241.9	0.120	0.39 ± 0.17	121.0	**0.79 ± 0.05**	0.088
	$S3^{MI}_{b0}$	613.1 ± 55.5	0.089	1702.0 ± 316.2	0.189	0.32 ± 0.16	940.0	0.58 ± 0.07	0.292
Strategy 4	$S4^{AMI}_{ADC}$	562.0 ± 41.4	0.100	1677.8 ± 213.4	0.140	0.47 ± 0.16	1.680	0.57 ± 0.09	2.700
	$S4^{AMI}_{b0}$	659.6 ± 71.1	0.080	1716.5 ± 277.4	0.140	0.16 ± 0.11	0.440	0.39 ± 0.12	0.080
Strategy 4'	$S4'^{AMI}_{ADC}$	505.3 ± 33.2	0.140	1585.0 ± 197.3	0.080	0.55 ± 0.14	0.140	0.63 ± 0.08	12.10
	$S4'^{AMI}_{b0}$	571.8 ± 61.3	0.140	1633.4 ± 224.6	0.140	0.41 ± 0.16	12.40	0.50 ± 0.15	0.280

The best performing strategy in terms of average for each criteria is highlighted in bold. P-value for each registration strategy and evaluation criterion, when compared to unregistered raw images is given.

$\mathcal{D}_{MI}$ and $\mathcal{D}_{AMI}$ (i.e., $S3$, $S4$, and $S4'$) scored higher in image mosaicing accuracy ($P < 0.05$, for all three image mosaicing accuracy evaluation criteria) while using ADC images instead of b0 images.

Moreover, the choice of the ADC instead of b0 image in the registration approach significantly improved the results of DWI to T_1 alignment accuracy for all strategies ($P < 0.05$). Figure 7 shows the influence of the image stations used on the multi-modal alignment for the same registration strategy.

Computation Times

Processing was performed using a 2,5 GHz Intel(R) Core(R) i7 processor and 16 GB RAM. The entire registration procedure (single threaded execution) for $S1$ ranged between 6 and 7 min. For $S2$ between 10 and 11 min. $S3$ and $S4$ were computationally considerably more expensive due to the separate deformable registrations of each DW segment onto anatomical whole-body reference in $S3$ and high computational demand of $\mathcal{D}_{AMI}$ metric in $S4$. In

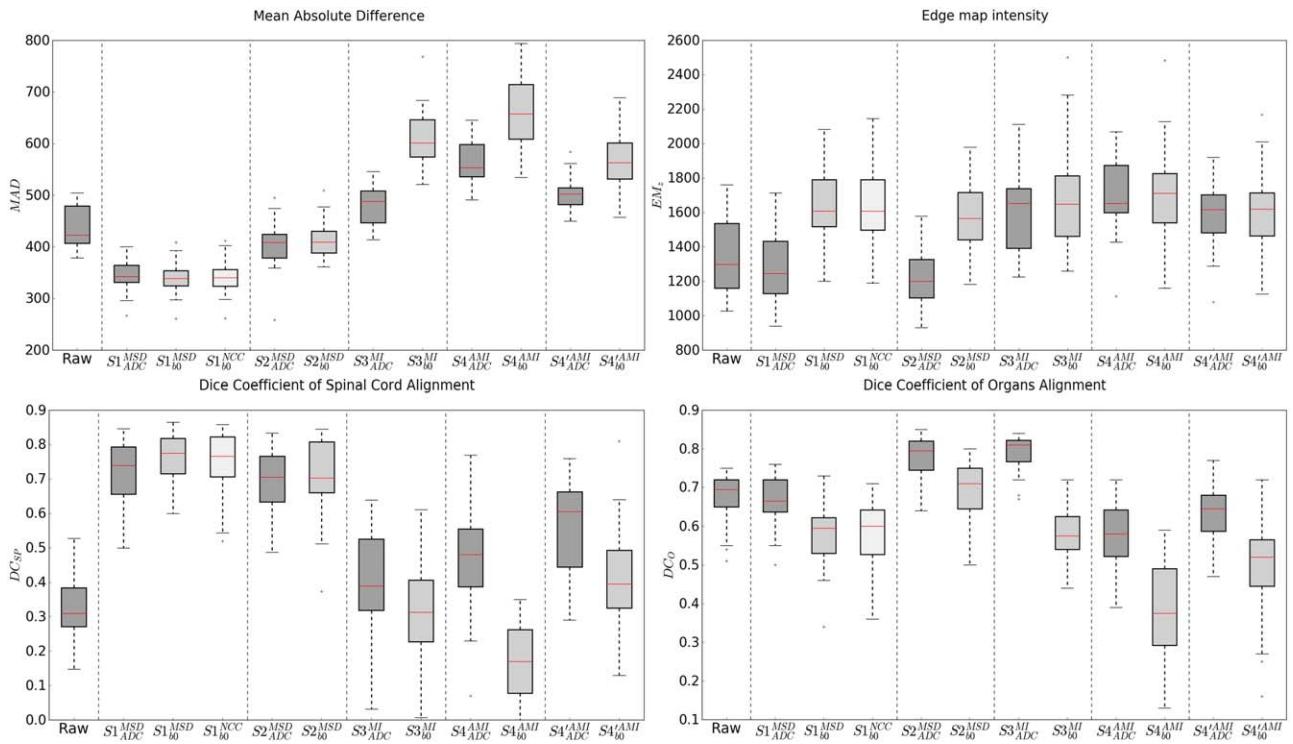

FIG. 4. Distribution of the results for different registration strategies. Four different validation methods were used to measure image registration accuracy.

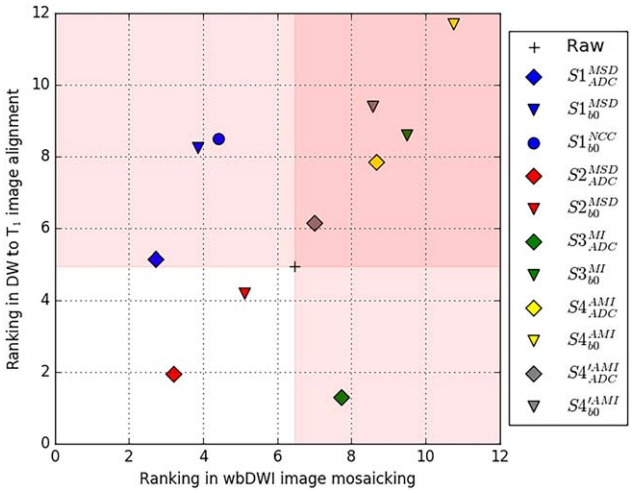

FIG. 5. Two dimensional averaged ranking number of the 11 registration strategies and raw, non-registered data in the 20 whole-body image sets. The lower the rank, the better the performance of the approach. Areas highlighted in light red indicate regions where no improvement is noted in either whole-body image quality or wbDWI alignment to T_1 or both (dark red), when compared to raw, non-registered images.

that case, the procedure lasted respectively 40–65 min ($S3$) and 100–180 min ($S4$), depending on the resolution of the MR image used.

DISCUSSION AND CONCLUSIONS

The results confirm the challenging nature of the addressed registration problem. Only one strategy ($S2^{\mathrm{MSD}}_{\mathrm{ADC}}$) led to improvement of all evaluation measures, when considering the average over all patients (Table 2). A similar conclusion can be drawn when ponderating wbDWI image mosaicing and T_1 alignment, considering the average rank (Fig. 5). Only $S2^{\mathrm{MSD}}_{\mathrm{ADC}}$ clearly demonstrated a benefit over no registration, with $S2^{\mathrm{MSD}}_{b0}$ only showing marginal improvement over no registration.

Two-step registration strategies $S1$ and $S2$ performed significantly better than strategies implemented as a one-step approach (i.e., $S3$ and $S4$) in terms of DWI mosaicing accuracy. Mosaicing the DWI stations separately, prior to the multi-modal registration, allowed to consistently improve wbDWI mosaicing accuracy. The improved performance is suspected to be due to the use of simpler, one-to-one metrics ($\mathcal{D}_{\mathrm{MSD}}$ or $\mathcal{D}_{\mathrm{AMSD}}$), advantageous when considering the poor DW image quality. The visual quality of the resulting images was also higher, with less visible discontinuities in the image station boundaries and no voxel shift artifacts, such as described by Koh et al. (14) (Fig. 6). Additional advantages of the two-step registration strategies $S1$ and $S2$ were the short computation times.

The results of multi-modal deformable alignment between wbDWI and whole-body T1 are less conclusive. Strategy $S3^{\mathrm{MI}}_{\mathrm{ADC}}$ marginally outperformed $S2^{\mathrm{MSD}}_{\mathrm{ADC}}$ in terms of DC_O of the segmented organs. Strategies using the mutual information metric or its variation D_{AMI} for wbDWI image mosaicing were found to be unstable and did not improve mosaicing results neither in rigid, nor the deformable step. On the other hand, groupwise two-step $S2$ strategy, not only improved wbDWI stations alignment but also multi-modal image alignment, in contrast to $S1$, which resulted only in wbDWI mosaicing accuracy improvement.

Mosaicing performed by pairwise registration in strategy $S1$ may have resulted in the accumulation of registration errors, and excessive image tilting towards the front, hampering subsequent wbDWI to T_1 deformable registration. The process of minimizing the global transformation between the neighbouring stations by a groupwise metric in $S2$, not only provides a highly accurate image mosaicing in wbDWI image, but also avoids excessive tilting, which was confirmed visually.

Joint optimization approaches, such as groupwise approaches $S4$ and $S4'$, carry the advantage of considering all degrees of freedom simultaneously. As a downside, since the cost function may contain more local minima, they could be more sensitive to initialization. For the results reported, strategies $S1$, $S2$, $S3$, and $S4$ were initialized starting from the raw, non-registered image positions. To investigate the influence of the initialization, we verified the performance of the multi-modal groupwise strategy as used in $S4$, when initialized with the result of the best performing strategy $S2^{\mathrm{MSD}}_{\mathrm{ADC}}$. The results of latter strategy $S4'$ led to significant improvement with respect to $S4$. However, it did not further improve the results of $S2^{\mathrm{MSD}}_{\mathrm{ADC}}$ from which it was initialized. Further investigation revealed that the multi-modal groupwise metric value D_{AMI} returned a better final cost function value for the $S4'$ than for the same metric for the result of $S2^{\mathrm{MSD}}_{\mathrm{ADC}}$, demonstrating the registration was indeed able to identify a better solution in terms of the metric value. However, the evaluation criteria for $S4'$ showed that the obtained result was inferior in terms of whole-body image quality, which was confirmed visually. The reconstructed whole-body images consistently bore strong, unnatural image deformations. We therefore hypothesize that the problem of $S4$ lies in the complexity of the multi-modal groupwise metric D_{AMI}. It is likely that this metric displays ill-defined optima, and therefore led the registration away from the accurate alignment, even when properly initialized. A superior multi-modal groupwise metric could improve the performance of strategies $S4$ and $S4'$. However, the development of such a metric is out of the scope of this work.

Lastly, the use ADC or b0 images did not influence image mosaicing accuracy for strategy $S2$, however, the direct registration strategies ($S3$ and $S4$) represented higher DWI alignment accuracy where registration was driven by the ADC image. Moreover, the choice of the ADC instead of b0 image in the registration approach improved the results of DWI to T_1 alignment accuracy for each strategy. Such a difference in mosaicing and multi-modal registration performance accuracy may be explained by a residual intensity bias present between b0 stations after intensity standardization correction. ADC maps are less susceptible to intensity scale differences between stations, T_2 shine-through artefacts and intensity values are less dependent on the DWI imaging sequence used. Deformable approaches guided by b0 images hold too little relevant image information and

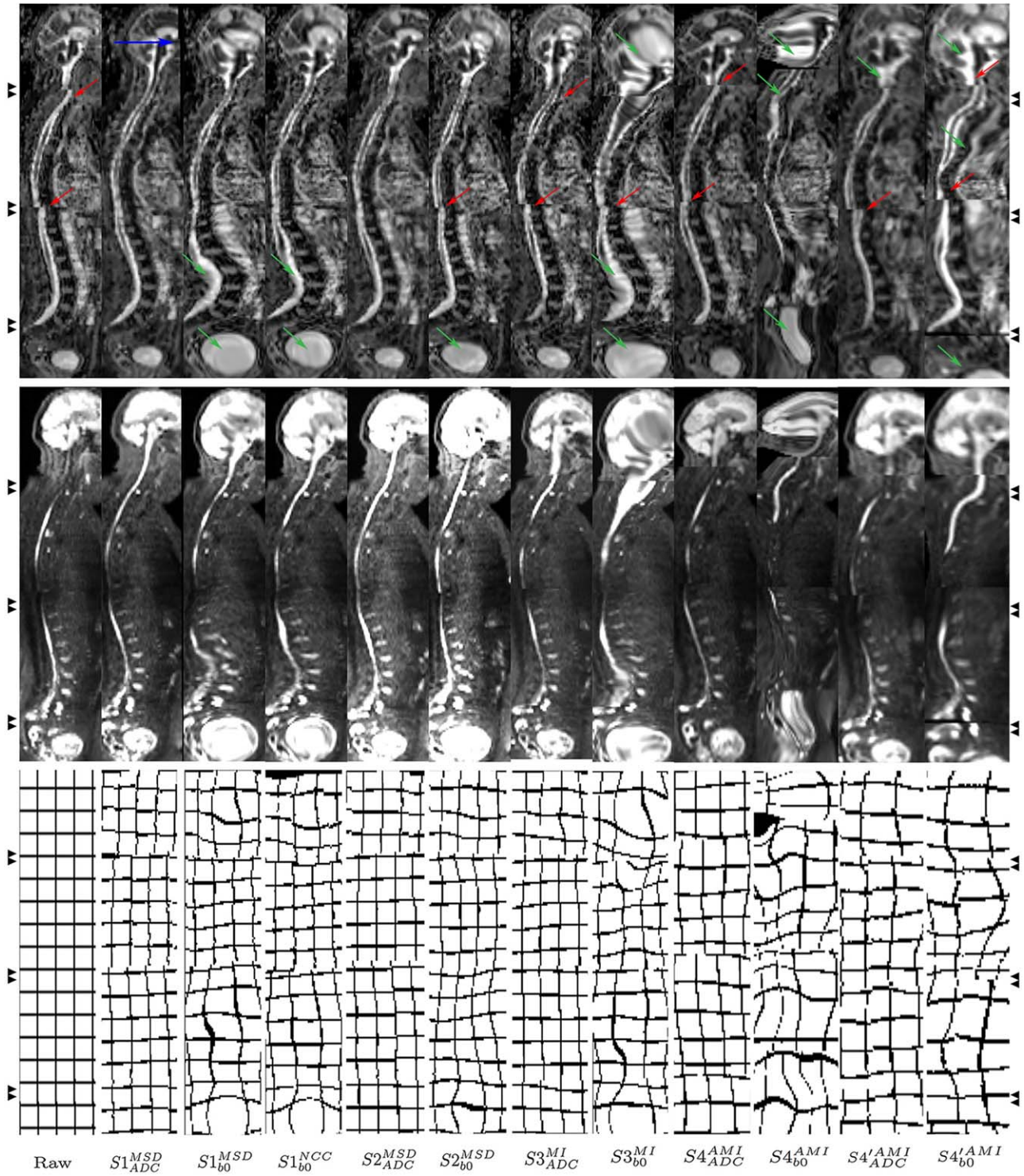

FIG. 6. Top: Reconstructed whole-body ADC volumes and diffusion-weighted b1000 images for each of the proposed strategies. The same slice from each 3D volume is shown in sagittal plane. Strategy *S2* based on ADC images shows the best quality of wbDWI image. Red arrows indicate image discontinuities between the stations, green - unnatural image deformations and blue image tilt towards the frontal side. The inter-station overlap region is indicated by markers on the sides. Bottom: Corresponding image deformation grids.

often are not regularized enough, and for that reason, introduce strong image deformations (see Fig. 6). Therefore, it is beneficial to use ADC images over b0 images, which provide not only high wbDWI mosaicing accuracy, but also precise alignment to anatomical whole-body counterpart.

Additionally, the influence of the number of *b*-values used to calculate ADC maps on the proposed registration strategies was investigated. For subjects with 3 or 4 *b*-values ($n=13$), the ADC maps were calculated using only 2 *b*-values (i.e., $b=0$ and $b=1000$ s/mm^2). The results for all ADC-based registration strategies (i.e.,

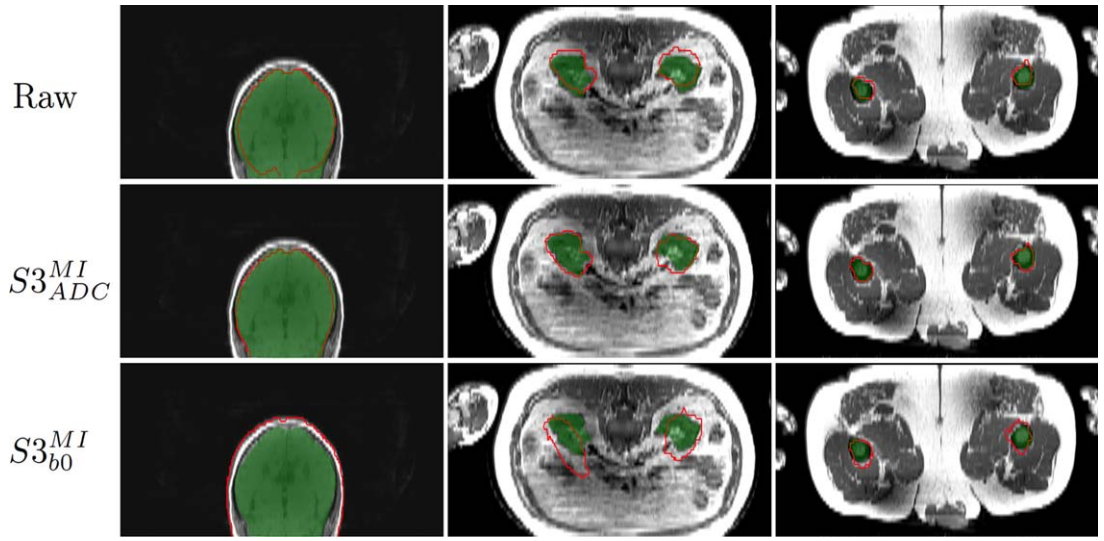

FIG. 7. Organs segmented from DWI stations (red) aligned with organs segmented from the T_1 whole-body image (green) before and after the registration process. The same slice from each 3D volume covering brain (left), kidneys (middle), and femur bones (right) is shown in the axial plain. The influence of the used image (ADC or b0) is presented for the same method (S3). Strategies driven by ADC image stations showed higher T_1 to DWI registration accuracy. Unnatural image deformations were present in methods using b0 images.

$S1^{\mathrm{MSD}}_{\mathrm{ADC}}$, $S2^{\mathrm{MSD}}_{\mathrm{ADC}}$, $S3^{\mathrm{MI}}_{\mathrm{ADC}}$, and $S4^{\mathrm{AMI}}_{\mathrm{ADC}}$) showed marginally worse performance than techniques driven by the ADC maps computed by all available *b*-values, however the difference was not statistically significant ($P > 0.05$).

A number of study limitations should be mentioned. First, mosaicing of the T_1 image stations was not investigated, because the quality of the whole-body image provided by the scanner vendor was excellent. Previous work by our group and other authors showed that, because of high image resolution and SNR, stitching of such anatomical image stations can be accurately performed using pairwise rigid or even deformable registration (27) of the station overlap.

Secondly, our methodology requires the whole-body MR acquisition sequence to be acquired with station overlap. For sequences with no overlap, adapted approaches should be investigated. Similarly, many centres acquire anatomical images with a different contrast (e.g., T_2-weighted or Dixon images), and the performance of the proposed method for such sequences should also be evaluated in future experiments.

Despite of the extensive experimentation performed, it is possible that unexplored combinations of similarity metrics, used images or registration parameters could lead to better performance of certain registration strategies.

Finally, the registration was applied only on the Philips scanner data. There may be differences in contrast and image quality between different vendors, which may influence the results.

In conclusion, in this work we have investigated four registration strategies for the formation of wbDWI image and its alignment to the whole-body T_1 anatomical reference. Two-step approaches showed superior DWI mosaicing performance over direct approaches. Moreover, when performed using a groupwise scheme (*S2*), which allowed for the minimization of the global image transformation, two-step approaches also allowed for accurate alignment to the whole-body anatomical counterpart. This registration strategy led to an improvement of the quality of the whole-body DW image and multimodal alignment with respect to the unregistered image, in terms of all evaluated measures.

ACKNOWLEDGMENTS

This work was supported by Innoviris: Platform for Imaging in Clinical Research in Brussels (PICRIB) project.

REFERENCES

1. Namasivayam S, Martin DR, Saini S. Imaging of liver metastases: MRI. Cancer Imaging 2007;7:2.
2. Baur-Melnyk A, Buhmann S, Dürr H, Reiser M. Role of MRI for the diagnosis and prognosis of multiple myeloma. Eur J Radiol 2005;55:56–63.
3. Weininger M, Lauterbach B, Knop S, Pabst T, Kenn W, Hahn D, Beissert M. Whole-body MRI of multiple myeloma: comparison of different MRI sequences in assessment of different growth patterns. Eur J Radiol 2009;69:339–345.
4. Kwee TC, Ludwig I, Uiterwaal CS, van Ufford HMQ, Vermoolen MA, Fijnheer R, Bierings MB, Nievelstein RA. ADC measurements in the evaluation of lymph nodes in patients with non-hodgkin lymphoma: feasibility study. Magn Reson Mater Phys Biol Med 2011;24:1–8.
5. Darge K, Jaramillo D, Siegel MJ. Whole-body MRI in children: current status and future applications. Eur J Radiol 2008;68:289–298.
6. Koh D-M, Collins DJ. Diffusion-weighted MRI in the body: applications and challenges in oncology. Am J Roentgenol 2007;188:1622–1635.
7. Lecouvet FE, El Mouedden J, Collette L, Coche E, Danse E, Jamar F, Machiels J-P, Berg BV, Omoumi P, Tombal B. Can whole-body magnetic resonance imaging with diffusion-weighted imaging replace Tc 99m bone scanning and computed tomography for single-step detection of metastases in patients with high-risk prostate cancer? Eur Urol 2012;62:68–75.
8. Padhani AR, Makris A, Gall P, Collins DJ, Tunariu N, de Bono JS. Therapy monitoring of skeletal metastases with whole-body diffusion MRI. J Magn Reson Imaging 2014;39:1049–1078.
9. Blackledge MD, Collins DJ, Tunariu N, Orton MR, Padhani AR, Leach MO, Koh D-M. Assessment of treatment response by total tumor volume and global apparent diffusion coefficient using diffusion-weighted MRI in patients with metastatic bone disease: a feasibility study. PLoS One 2014;9:e91779–e91704.

10. Giles SL, Messiou C, Collins DJ, Morgan VA, Simpkin CJ, West S, Davies FE, Morgan GJ, deSouza NM. Whole-body diffusion-weighted MR imaging for assessment of treatment response in myeloma. Radiology 2014;271:785–794.
11. Jäger F, Hornegger J. Nonrigid registration of joint histograms for intensity standardization in magnetic resonance imaging. IEEE Trans Med Imaging 2009;28:137–150.
12. Nyúl LG, Udupa JK, Zhang X. New variants of a method of MRI scale standardization. IEEE Trans Med Imaging 2000;19:143–150.
13. Dzyubachyk O, Staring M, Reijnierse MM, Lelieveldt BP, van der Geest RJ. Inter-station intensity standardization for whole-body MR data. Magn Reson Med 2016;77:422–433.
14. Koh D-M, Blackledge M, Padhani AR, Takahara T, Kwee TC, Leach MO, Collins DJ. Whole-body diffusion-weighted MRI: tips, tricks, and pitfalls. Am J Roentgenol 2012;199:252–262.
15. Takahara T, Imai Y, Yamashita Y, Yasuda T, Nasu SS, Van Cauteren M. Diffusion weighted whole body imaging with background body signal suppression (DWIBS): technical improvement using free breathing, STIR and high resolution 3D display. Matrix 2004;160:160.
16. Dzyubachyk O, Lelieveldt BP, Blaas J, Reijnierse M, Webb A, van der Geest RJ. Automated algorithm for reconstruction of the complete spine from multistation 7T MR data. Magn Reson Med 2013;69:1777–1786.
17. Bhatia KK, Hajnal J, Hammers A, Rueckert D. Similarity metrics for groupwise non-rigid registration. In International Conference on Medical Image Computing and Computer-Assisted Intervention. Berlin: Springer; 2007. pp. 544–552.
18. Rueckert D, Sonoda LI, Hayes C, Hill DL, Leach MO, Hawkes DJ. Nonrigid registration using free-form deformations: application to breast MR images. IEEE Trans Med Imaging 1999;18:712–721.
19. Joshi S, Davis B, Jomier M, Gerig G. Unbiased diffeomorphic atlas construction for computational anatomy. NeuroImage 2004;23:S151–S160.
20. Maes F, Collignon A, Vandermeulen D, Marchal G, Suetens P. Multimodality image registration by maximization of mutual information. IEEE Trans Med Imaging 1997;16:187–198.
21. Polfliet M, Klein S, Huizinga W, de Mey J, Vandemeulebroucke J. The pythagorean averages as group images in efficient groupwise registration. In 2016 IEEE 13th International Symposium on Biomedical Imaging (ISBI). Prague: IEEE, 2016. pp. 1261–1264.
22. Ceranka J, Polfliet M, Lecouvet F, Michoux N, de Mey J, Vandemeulebroucke J. Registration strategies for whole-body diffusion-weighted MRI stitching. In Computational diffusion MRI. Berlin: Springer, 2016. pp. 195–206.
23. Pasoglou V, Michoux N, Peeters N, Larbi F, Tombal A, Selleslagh B, Omoumi TP, Vande Berg BC, Lecouvet FE. Whole-body 3D T1-weighted MR imaging in patients with prostate cancer: feasibility and evaluation in screening for metastatic disease. Radiology 2014;275:155–166.
24. Ibanez L, Schroeder W, Ng L, Cates J. *The ITK Software Guide*. Kitware, Inc. second ed. ISBN 1-930934-15-7, http://www.itk.org/ItkSoftwareGuide.pdf, 2005.
25. Klein S, Staring M, Murphy K, Viergever MA, Pluim JP. Elastix: a toolbox for intensity-based medical image registration. IEEE Trans Med Imaging 2010;29:196–205.
26. Shapiro SS, Wilk MB. An analysis of variance test for normality (complete samples). Biometrika 1965;52:591–611.
27. Wachinger C, Glocker B, Zeltner J, Paragios N, Komodakis N, Hansen M.S., Navab N. Deformable mosaicing for whole-body MRI. In International Conference on Medical Image Computing and Computer-Assisted Intervention. Berlin: Springer, 2008. pp. 113–121.